Abstract

For the most part, the study of dendritic crystal growth has focused on continuum models featuring surface energies that yield six pointed dendrites. In such models, the growth shape is a function of the surface energy anisotropy, and recent work has shown that considering a broader class of anisotropies yields a correspondingly richer set of growth morphologies. Motivated by this work, we generalize nanoscale models of dendritic growth based on kinetic Monte Carlo simulation. In particular, we examine the effects of extending the truncation radius for atomic interactions in a bond-counting model. This is done by calculating the model's corresponding surface energy and equilibrium shape, as well as by running KMC simulations to obtain nanodendritic growth shapes. Additionally, we compare the effects of extending the interaction radius in bond-counting models to that of extending the number of terms retained in the cubic harmonic expansion of surface energy anisotropy in the context of continuum models.

Dendritic Growth Shapes in Kinetic Monte Carlo Models

Tim R. Krumwiede,Tim P. Schulze

December 8, 2016

1 Introduction

Dendritic growth has been studied extensively from both an experimental and theoretical point of view. This intense study is due to fundamental scientific interest as well as the importance of this striking phenomenon from a technological point of view. The vast majority of dendrite simulations have used continuum models aimed at macroscale solid-liquid interfaces, e.g. a pure solid growing into its melt. In this paper, we seek to build upon the smaller body of work that has examined dendritic growth on atomistic length scales using kinetic Monte Carlo (KMC) simulation. These models are best suited to growth from vapor with low concentrations of the growth species. Interfaces where a solid is in equilibrium with its melt tend to be at much higher temperature and pressure than interfaces where a vapor is in equilibrium with a solid. Thus, our simulations correspond to lower temperatures, with a correspondingly lower entropic contribution to the surface free energy and crystal surfaces that tend to be more faceted.

While the growth of a snowflake is a familiar example of this regime, KMC studies have tended to focus on more idealized systems, most often the growth of simple cubic crystals. These studies include the work of Witten and Sander on diffusion limited aggregation [1]. To simulate more structured dendritic growth one must include a surface diffusion mechanism. For simple cubic growth, this has been examined in a number of two-dimensional studies [2, 3, 4, 5], and at least one study of three-dimensional growth [6].

More recently, Schulze [7] has examined KMC simulation of FCC dendrites. This model aims to examine the growth of a dendrite into an under-cooled melt using a hybrid KMC-continuum model where the thermal diffusion was simulated using the heat equation discretized on the FCC lattice. From the nanoscale perspective, this has the disadvantage of removing thermal fluctuations from the model. In contrast, our present work will consider instead the growth of a dendrite from a super-saturated vapor, modeled as a lattice gas at constant temperature. The bulk diffusion of the precipitating species is then readily simulated with a random walk, so that the fluctuations in the growth process can be more consistently modeled.

Our aim here is to examine a broader class of KMC models capable of capturing a wider range of dendrite morphology. We were initially motivated by the work of Haxhimali et. al. [8] who have pointed out that the vast majority of work using continuum models has

been aimed at the growth of FCC and other cubic dendrites with primary growth occurring along the six faces of the cubic unit cell. In particular, their work emphasizes the potential for moving continuously from $\langle 100 \rangle$- to $\langle 110 \rangle$-oriented growth as one varies composition-dependent surface energy parameters. According to their model, this would result in a transition from six- to twelve-armed dendrites with a variety of complicated and fascinating hybrid structures in between.

Haxhimali et al. [8] base their conclusions on phase field simulations of a continuum model with a truncated expansion of the anisotropy in the interfacial free-energy, $\gamma(\theta, \phi)$, in terms of "cubic harmonics" [9], K_1 and K_2, which are formed from linear combinations of spherical harmonics $Y_{lm}(\theta, \phi)$ to reflect the symmetry of cubic crystals:

$$\gamma(\theta, \phi) \approx \gamma_0[1 + \epsilon_1 K_1(\theta, \phi) + \epsilon_2 K_2(\theta, \phi)]. \tag{1}$$

The coefficients, ϵ_1 and ϵ_2, are material-dependent anisotropy parameters. The authors note that essentially all prior studies retain only the $\epsilon_1 K_1$-term that favors the ubiquitous $\langle 100 \rangle$ dendrite, and point to an earlier Molecular Dynamics (MD) study of Asta et. al. [9] that suggests the $\epsilon_2 K_2$-term, which favors $\langle 110 \rangle$-oriented growth, is significant for a wide range of FCC metals. They support their theory with both simulations of the continuum model for dendritic growth into an under-cooled melt and directional solidification experiments of $\mathrm{Al-Zn}$ alloys. The experiments study the surface energy anisotropy by considering varying amounts of Zn, and support the numerical study. We seek a similar generalization for KMC studies of crystal growth aimed at the nanoscale.

In the next section we start with a broad introduction to KMC before turning to the specific model used for the present study. In Section 3 we derive the surface energy for our model, and in Section 4 we examine the corresponding equilibrium shapes as well as the growth shapes that emerge as the result of simulation. In Section 5 we discuss the relationship with the work of Haxhimali et al. and some important distinctions between the continuum and KMC models.

2 Kinetic Monte-Carlo

KMC models usually take the form of discrete-space, continuous-time Markov processes, where the system passes through a sequence of states $\{\mathbf{x}_{\alpha_n} \in \mathcal{X}\}$ drawn from a model dependent state-space $\mathcal{X} = \{\mathbf{x}_\alpha = \{x_{ijk} \in \{0, 1\}\}\}$ at transition times $\{t_n\}$. Here α is a discrete index used to enumerate the possible states. The states themselves, $\mathbf{x}_\alpha$, take the form of an occupation array for some set of lattice points, with 1 signifying occupied and 0 unoccupied. In this paper, for example, we consider an arbitrary Bravais lattice $\{i\mathbf{a}_1 + j\mathbf{a}_2 + k\mathbf{a}_3\}$ defined by a set of primitive vectors $\{\mathbf{a}_1, \mathbf{a}_2, \mathbf{a}_3\}$.

In KMC, the transition matrix for the Markov process is typically sparse, with rates $R_{\alpha\beta} = 0$ except for certain local transitions. In this paper, we consider models that are mostly limited to the exchange of neighboring occupied and unoccupied lattice sites. In other words, every transition on the interior of the domain consists of a single atom moving to an unoccupied site. The transition rates $R_{\alpha\beta}$ are chosen so that an equilibrium simulation

will achieve the Boltzmann distribution:

$$\rho(\mathbf{x}) = Z^{-1} \exp\left(-\frac{E(\mathbf{x})}{k_b T}\right), \quad Z = \sum_{x \in \mathcal{X}} \exp\left(-\frac{E(\mathbf{x})}{k_b T}\right), \tag{2}$$

where $\rho(\mathbf{x})$ is the probability of finding the system in state $\mathbf{x}$, $E(\mathbf{x})$ is a discrete Hamiltonian associating an energy with each possible state, Z is the canonical partition function, k_b is the Boltzmann constant, and T is the temperature, which we take to be uniform across the system.

A simple and conventional way of enforcing the correct equilibrium distribution in (2) is to impose a condition of *detailed balance*:

$$\rho(\mathbf{x}_\alpha) R_{\alpha\beta} = \rho(\mathbf{x}_\beta) R_{\beta\alpha}, \tag{3}$$

which matches the flux between any two states. A common choice for the rates $R_{\alpha\beta}$ that satisfies (3) and that is motivated by Transition State Theory [10] is

$$R_{\alpha\beta} = K \exp\left(-\frac{E(\mathbf{x}_\alpha) - E_{\alpha\beta}}{k_b T}\right), \tag{4}$$

where the prefactor K is normally taken to be a constant and $E_{\alpha\beta}$ is the energy of the "transition state". In a model based on an empirical potential, where particles can occupy an arbitrary point in configuration space, the transition state is identified with the energy at saddle points on the energy landscape. In a lattice-based model, there are no such points and we simply define $E_{\alpha\beta}$ to play an analogous role. In many bond-counting models, including those considered here, $E_{\alpha\beta}$ can be thought of as the energy of the system with the transitioning atom removed. Equivalently, the energy barrier $E(\mathbf{x}_\alpha) - E_{\alpha\beta}$ is defined to be the interaction energy between the atom being moved and the rest of the system.

2.1 KMC Simulation of Dendritic Growth

For our present simulations, we imagine a vapor solution initially at a uniform concentration and a temperature that will remain constant. The domain is a sphere of fixed radius, large enough that this concentration may be assumed fixed at the boundary of the sphere. The precipitate is nucleated in a much smaller sphere at the center of the domain (see Fig. 1). Growth occurs as particles precipitate and diffuse along the surface of the crystal, which depletes the concentration of the solidifying species in a boundary layer that conforms to the crystal surface. This depletion of the precipitating species provides the driving force for a Mullins-Sekerka-type morphological instability [11], as protruding portions of the surface have access to a richer concentration of the growth species in the far-field.

More specifically, our simulations use a large FCC lattice within a spherical domain with a radius of approximately 200 lattice spacings. An occupied lattice site represents an atom of the growth species, whereas an empty site represents the medium from which the dendrite is growing. The diffusion of the growth species from the far-field to the crystal surface is modeled as a random walk on an FCC lattice with subsequent attachment and surface diffusion. An alternative model with an off-lattice random walk was also considered, but rejected in favor of the more readily implemented discrete model. Initially, all nodes within

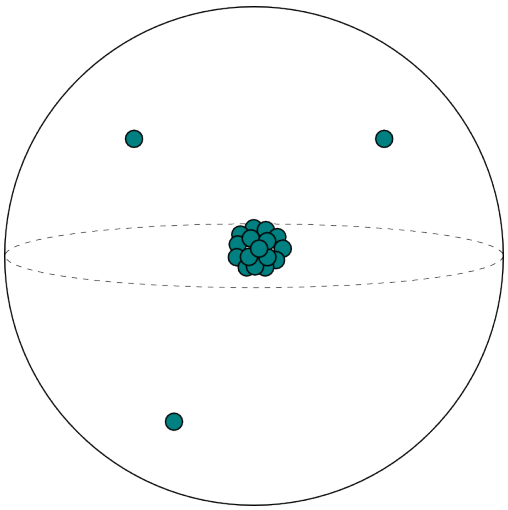

Figure 1: An illustration of the simulation domain, nucleated growth species in the center, and adatoms diffusing through the far-field.

five lattice spacings from the center are considered occupied, constructing a small cluster with about 600 atoms.

In principle, each atom shares interactions with all other atoms in the system. However, in our simulations, interactions are limited to a finite number of pairwise "bonds." Since every node in a Bravais lattice has neighbors in the same directions, each bond can be represented by a vector between nodes of the lattice: $\mathbf{v} = v_1\mathbf{a}_1 + v_2\mathbf{a}_2 + v_3\mathbf{a}_3$ with $v_i \in \mathbb{Z}$. Without loss of generality, we will arbitrarily associate these bonds with one of the two interacting atoms by choosing an orientation for $\mathbf{v}$, and denote the set of bonds for a given model as $\{\mathbf{v}_j\}$.

The energy $E(\mathbf{x})$ is given by

$$E(\mathbf{x}) = -\frac{1}{2}\sum_{i=1}^{n_a}\sum_{j=1}^{n_b} w_j N_j(i), \tag{5}$$

where n_a is the number of atoms, n_b is the number of bond types $\{\mathbf{v}_j\}$, w_j is the weight corresponding to $\mathbf{v}_j$ or the energy value of a $\mathbf{v}_j$ bond, and $N_j \in \{0, 1, 2\}$ is the number of bonds an atom shares with its neighbors with either $\mathbf{v}_j$ or $-\mathbf{v}_j$ orientation.

The transition rate $R_{\alpha\beta}$ for the surface diffusion process depends solely on how many bonds it shares with neighbors. The rate for an atom moving to an open site is given by

$$R = K \exp\left(-\frac{1}{k_b T}\sum_{j=1}^{n_b} w_j N_j\right).$$

In the models we will consider, many of the bonds share the same weight.

The KMC simulation is implemented using the inverted list algorithm described in [12]. At each iteration of the simulation either a single atom moves to an adjacent site on the lattice or a new atom is generated on the domain boundary. The rates for atom movement events, denoted $R_{n_1 n_2}$, are a function of the number of occupied nearest- and next-nearest-neighbor sites which are n_1 and n_2 respectively. Additionally, we need a counter $a_{n_1 n_2}$ telling

us the number of events with rate $R_{n_1 n_2}$ in the current configuration. Finally, there is one additional rate g representing the uniform flux of the growth species from the far-field.

Our simulations are performed with two different boundary conditions. When growing a dendrite, atoms are deposited onto boundary sites at a uniform rate and annihilated upon moving onto a boundary site, so that a uniform far-field concentration is maintained. When finding equilibrium shapes, all flux at the boundary is removed by setting $g = 0$ and reflecting atoms that move onto a boundary site, so that the number of atoms n_a is conserved.

3 Surface Energy in Bond-Counting Models

To gain insight into the equilibrium behavior of the bond-counting model just described, we first derive the corresponding surface energy function, $\gamma_b(\hat{\mathbf{n}})$, which we define as the number of broken bonds per unit area along a surface with normal $\hat{\mathbf{n}}$. Note that, in contrast to (1) this is a zero-temperature surface energy rather than a free-energy. In the KMC simulations, the entropic effects due to finite temperature are controlled via the rates (4), whereas in a continuum model they are modeled through the choice of γ, e.g. (1). Derivation of the surface energy function of bond-counting models for FCC metals has been demonstrated in previous studies for bonds up to a specified truncation radius [13, 14, **?**]. Here we adopt an approach advocated in a footnote in Mackenzie et al. [13], providing details for any set of bonds on any Bravais lattice.

We calculate the total surface energy for a facet with normal $\hat{\mathbf{n}}$ by computing the contribution of each $\mathbf{v} \in \{\mathbf{v}_j\}$ individually. A 2D example of this is shown in Fig. 2, along with a facet cutting bonds associated with the same vector $\mathbf{v}$. It is important to note that, depending on the length of $\mathbf{v}$, bonds between atoms may overlap. This happens if and only if $z \equiv \gcd(v_1, v_2, v_3) > 1$ where gcd denotes the greatest common divisor. Note that z is the density of overlapping $\mathbf{v}$ bonds.

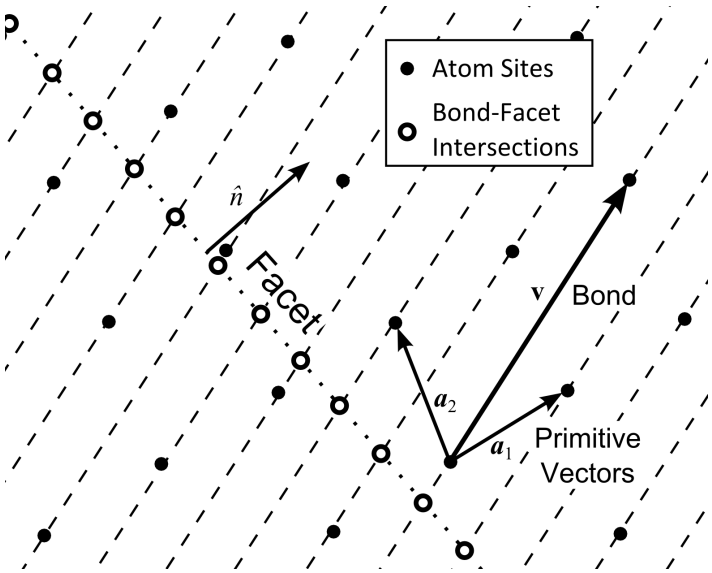

Figure 2: An illustration in two dimensions of a Bravais lattice, its two primitive vectors, a bond vector $\mathbf{v}$, a facet with normal $\hat{\mathbf{n}}$, and the collection of bond-facet intersections. The latter forms a Bravais lattice in one fewer dimensions along the facet.

First, we show that on a 3D Bravais lattice, the intersections of bonds corresponding to a vector $\mathbf{v}$ with a planar facet form a 2D Bravais lattice on the facet. Choose vectors $\tilde{\mathbf{a}}_1, \tilde{\mathbf{a}}_2$ such that the set $\{\mathbf{v}, \tilde{\mathbf{a}}_1, \tilde{\mathbf{a}}_2\}$ spans the crystal lattice. Each of the bonds corresponding to $\mathbf{v}$ lies on a line of the form $\{t\mathbf{v} + k_1\tilde{\mathbf{a}}_1 + k_2\tilde{\mathbf{a}}_2 + k\mathbf{v} \mid k, k_i \in \mathbb{Z}, t \in \mathbb{R}\}$ as shown in Fig. 2. To find the intersections of these lines and the facet given by $\{\mathbf{x} \mid \hat{\mathbf{n}} \cdot (\mathbf{x} - \mathbf{x}_0) = 0\}$ we solve the equation

$$\hat{\mathbf{n}} \cdot (t\mathbf{v} + \sum_{i=1}^{2} k_i\tilde{\mathbf{a}}_i + k\mathbf{v} - \mathbf{x}_0) = 0.$$

Solving for t gives

$$t = \frac{\hat{\mathbf{n}} \cdot \mathbf{x}_0}{\hat{\mathbf{n}} \cdot \mathbf{v}} + k - \sum_{i=1}^{2} k_i \frac{(\hat{\mathbf{n}} \cdot \tilde{\mathbf{a}}_i)}{\hat{\mathbf{n}} \cdot \mathbf{v}}.$$

Then the set of intersections can be written

$$\left\{ \sum_{i=1}^{2} k_i \frac{(\hat{\mathbf{n}} \cdot \mathbf{v})\tilde{\mathbf{a}}_i - (\hat{\mathbf{n}} \cdot \tilde{\mathbf{a}}_i)\mathbf{v}}{\hat{\mathbf{n}} \cdot \mathbf{v}} + \frac{\hat{\mathbf{n}} \cdot \mathbf{x}_0}{\hat{\mathbf{n}} \cdot \mathbf{v}}\mathbf{v} \quad \middle| \quad k_i \in \mathbb{Z} \right\}.$$

Therefore, the set of intersections is generated by integer combinations of the two vectors $\left\{ \frac{(\hat{\mathbf{n}} \cdot \mathbf{v})\tilde{\mathbf{a}}_i - (\hat{\mathbf{n}} \cdot \tilde{\mathbf{a}}_i)\mathbf{v}}{\hat{\mathbf{n}} \cdot \mathbf{v}} \,\middle|\, i = 1, 2 \right\}$ and is then a 2D Bravais lattice.

Now, consider a bond-counting model on a Bravais lattice with bonds corresponding to a vector $\mathbf{v}$. In the case $z = 1$, bonds do not overlap. From above, we know that the bond intersections on the facet form a Bravais lattice so the area on the facet per intersection equals the area of a Voronoi cell of this lattice. Construct a prism centered on each $\mathbf{v}$ bond with the 2D Voronoi cell as its base and spanning the length of the bond. This is illustrated in a 2D analog for easier viewing in Fig. 3. These prisms tile $\mathbb{R}^3$ and correspond to exactly one atom of the 3D lattice and are therefore primitive cells and have volume $V = |\det A|$ where $A = [\mathbf{a_1}, \mathbf{a_2}, \mathbf{a_3}]$. The height of each cell in the direction of $\hat{\mathbf{n}}$ is $h = \text{proj}_{\hat{\mathbf{n}}} \mathbf{v} = |\hat{\mathbf{n}} \cdot \mathbf{v}|$. Therefore, the area per bond intersection on the facet is given by $h^{-1}V = \frac{|\det A|}{|\hat{\mathbf{n}} \cdot \mathbf{v}|}$.

When bonds do overlap, $z = \gcd(v_1, v_2, v_3) > 1$. Following the construction above yields prisms that overlap with density z. By dividing these cells into z disjoint prisms each with height $h = z^{-1}|\hat{\mathbf{n}} \cdot \mathbf{v}|$, we arrive at a cell that tiles $\mathbb{R}^3$ without overlapping and contains one node of the lattice. This cell is then a primitive cell with volume $V = |\det A|$, which determines the area of a Voronoi cell on the facet: $h^{-1}V = \frac{z \det A}{|\hat{\mathbf{n}} \cdot \mathbf{v}|}$. Then, since there are z bonds cut at each intersection, the number of bonds cut per unit area on a facet with normal $\hat{\mathbf{n}}$ is $z\frac{|\hat{\mathbf{n}} \cdot \mathbf{v}|}{z|\det A|} = \frac{|\hat{\mathbf{n}} \cdot \mathbf{v}|}{|\det A|}$. Therefore, for $z \geq 1$, the bonds cut per unit area by a planar facet with normal $\hat{\mathbf{n}}$ is given by

$$\gamma_b(\hat{\mathbf{n}}) = \frac{|\hat{\mathbf{n}} \cdot \mathbf{v}|}{|\det A|}. \tag{6}$$

In a model with multiple types of bonds, we can superimpose the contribution of each bond $\mathbf{v}_j$ using the corresponding weight w_j. Then the total surface energy for a facet with normal $\hat{\mathbf{n}}$ is

$$\gamma_b(\hat{n}) = \frac{\sum_{j=1}^{n_b} w_j |\hat{n} \cdot \mathbf{v}_j|}{|\det A|}. \tag{7}$$

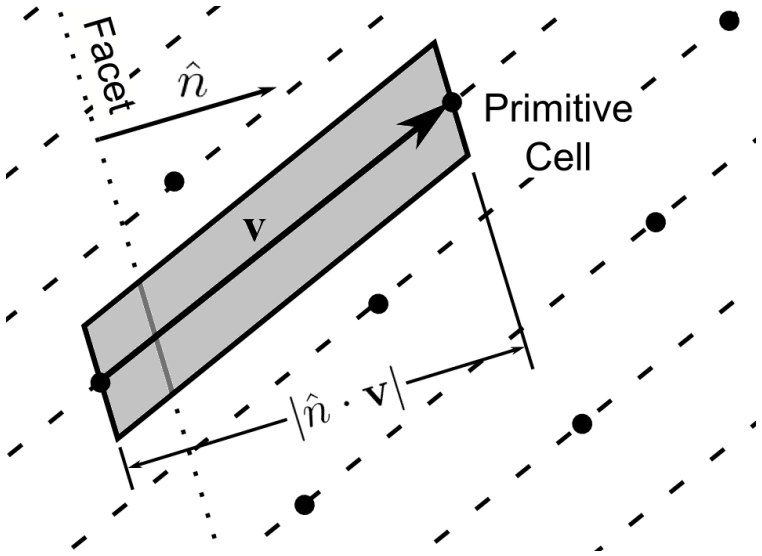

Figure 3: A 2D illustration of an arbitrary bond and a prismatic primitive cell with base parallel to a facet with normal $\hat{\mathbf{n}}$. In this case the Voronoi cell of facet intersections consists of a line segment and is shaded in the figure.

In the FCC examples that follow, the nearest-neighbor bonds share the weight w_1 and the next-nearest-neighbor bonds share the weight w_2. Surface energies for these examples take the form

$$\gamma_b(\hat{n}) = \frac{1}{|\det A|}\left(w_1 \sum_{i=1}^{6} |\hat{n} \cdot \mathbf{v}_{1i}| + w_2 \sum_{i=1}^{3} |\hat{n} \cdot \mathbf{v}_{2i}|\right), \tag{8}$$

where $\{\mathbf{v}_{1i}\}$ represent the bonds between FCC nearest-neighbors and $\{\mathbf{v}_{2i}\}$ the bonds between FCC next-nearest neighbors.

Fig. 4 contains examples of three-dimensional surface energies. Fig. 4a is the surface energy for a model counting nearest-neighbor bonds on a cubic lattice, each with weight $w = 1$. Fig. 4b counts nearest-neighbor bonds on a FCC lattice with weights $w_1 = 1, w_2 = 0$. Fig. 4b counts nearest- and next-nearest-neighbor on a FCC lattice with equal weights $w_1 = 1, w_2 = 1$.

4 Equilibrium and Growth Shape

A crystal in equilibrium is not subject to conditions that will drive its growth. The equilibrium shape minimizes the total surface energy among competitors with fixed volume:

$$\min_{|\Omega|=V} \int_{\mathbf{x}\in\partial\Omega} \gamma(\hat{n}(\mathbf{x}))dS. \tag{9}$$

The minimizer is also known as the Wulff shape and is given by the well-known formula [15]

$$W = \{\mathbf{x} \in \mathbb{R}^3 | \mathbf{x} \cdot \hat{\mathbf{n}} \leq \gamma(\hat{\mathbf{n}}) \, \forall \hat{\mathbf{n}}\}. \tag{10}$$

The surface of the Wulff shape can be described with the function

$$w(\hat{\mathbf{d}}) = \min_{\hat{\mathbf{d}}\cdot\hat{\mathbf{n}}>0} \left[\frac{\gamma(\hat{\mathbf{n}})}{\hat{\mathbf{d}} \cdot \hat{\mathbf{n}}}\right] \tag{11}$$

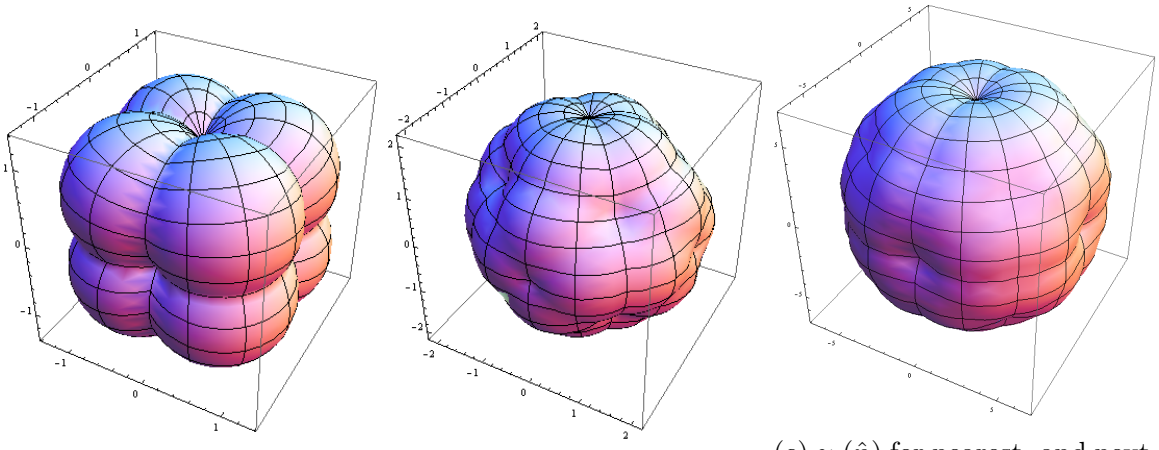

(a) $\gamma_b(\hat{n})$ for nearest-neighbor bonds on a cubic lattice

(b) $\gamma_b(\hat{n})$ for nearest-neighbor bonds on a FCC lattice

(c) $\gamma_b(\hat{n})$ for nearest- and next-nearest-neighbor bonds on a FCC lattice

Figure 4: Examples of Surface Energies

where $\left\{\hat{\mathbf{d}}\right\}$ is the set of all unit vectors. This shape is constructed by drawing planes which are orthogonal to the radius vector at each point on the spherical plot of $\gamma(\hat{\mathbf{n}})$ and taking the inner envelope of those planes.

As noted previously, the surface energy γ_b that we have derived for our bond-counting model is the zero-temperature surface energy. One result of this is that surface energies of the form (7) have several cusps. These cusps are local minima of the surface energies and lead to the faceted Wulff shapes seen in Fig. 6a & b. At nonzero temperatures, these cusps and the corresponding edges of the facets in equilibrium shapes become rounded. While we cannot directly compute this entropic contribution to the surface energy, we can simulate its effect on the equilibrium shape, as illustrated in Fig. 5. Calculating the Wulff shape is a useful tool for exploring the range of morphologies attainable within a given bond-counting model, as such calculations can be done with little effort compared to the lengthy simulations needed to generate the shapes shown in Fig. 5.

When a growing crystal is sufficiently small, surface diffusion will dominate the diffusive effects driving growth, so that the crystal evolves toward its equilibrium shape. The subsequent growth shape is more difficult to predict, but is heavily influenced by the equilibrium shape. For example, some crystals may have growth directions that correspond to faces of the Wulff shape while others may grow in directions corresponding to edges or vertices. One might think that if the growth directions correspond to faces, they would be the faces furthest from the center of the shape. Fig. 6 demonstrates that this is not always the case. The dendrite in Fig. 6c has six arms corresponding to square $\langle 100 \rangle$ facets of Fig. 6a, which are the furthest facets from the center of the Wulff shape. In Fig. 6d the eight arms correspond to the hexagonal $\langle 111 \rangle$ facets seen in Fig. 6b, but here we start to see that there are more complex mechanisms at play since the rectangular $\langle 110 \rangle$ facets are further away from the center and do not correspond to growth directions.

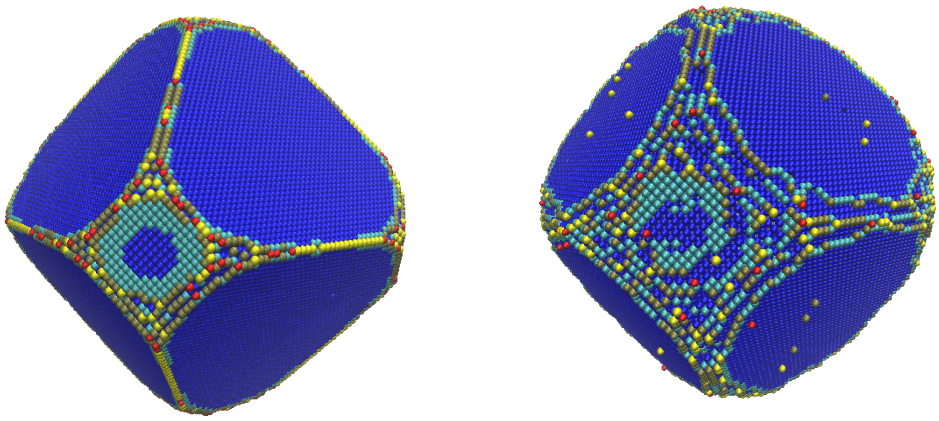

(a) Equilibrium Shape for $T = 351.7$ K (b) Equilibrium Shape for $T = 580.2$ K

Figure 5: KMC simulations of an FCC crystal's equilibrium shape counting only nearest-neighbor bonds under two different temperatures, with energy scaled such that $w_1 = 0.1$ eV. Higher temperatures lead to softer edges as seen in b. The corresponding surface energy for both of these models is shown in Fig. 4b.

5 Comparison with Continuum Models

Our aim here is to explore the role of anisotropic surface energy in our KMC model, denoted γ_b, guided by what is known about the influence of surface energy in the context of continuum models, which we now will denote γ_c. Due to significant differences between the two models and the physical scenarios they represent, no direct comparison is intended here. Rather, our focus is on the class of morphologies that can be exhibited within each model at a given level of approximation.

We start by reiterating the differences between the two models. For the most part, the dendritic growth of a pure material into its own melt is modeled using the heat equation along with appropriate boundary conditions. With some approximation, this can also be viewed as a model where the growth is occurring from a supersaturated vapor, a scenario that is more directly analogous to the KMC simulations described in the previous section. There is an extensive literature that examines the effects of both solute and heat diffusion on such processes [16]. More significantly, we have already commented on the important distinction that γ_b is a zero-temperature surface energy, while γ_c represents the free energy at the melting temperature. Another important distinction between the KMC simulations and simulations based on the continuum model, is that the former are necessarily restricted to atomistic length scales due to computational requirements, whereas the latter are largely aimed at the macroscale. While most studies of dendritic growth are done on scales larger than can be simulated with KMC, there are experimental results that exhibit nanodendrites with highly developed branches with length scales similar to our simulations [17, 18].

Despite these differences, it is natural to wonder whether or not similar growth shapes can be exhibited in both models and, if not, why? Of particular interest is the possibility of 12-armed and 24-armed dendrites. While we were able to find evidence for the latter, we were not able to exhibit 12-armed dendrites using a nearest- and next-nearest-neighbor bond-

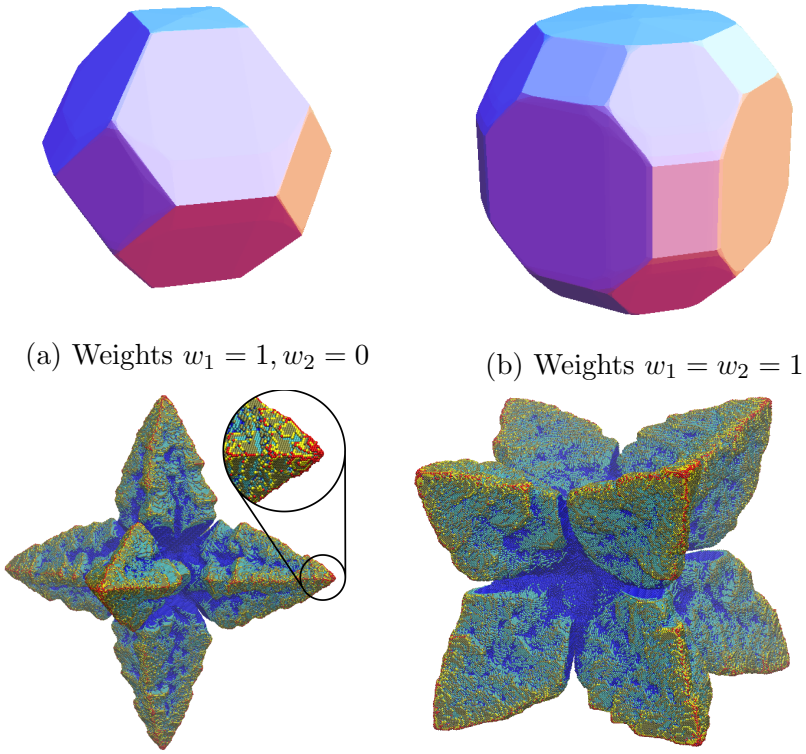

(a) Weights $w_1 = 1, w_2 = 0$

(b) Weights $w_1 = w_2 = 1$

(c) Six-armed dendrite

(d) Eight-armed dendrite

Figure 6: FCC Wulff shapes and the corresponding results of a KMC simulation on an FCC lattice. The Wulff shapes in a & b correspond to the surface energies in Fig. 4b and c, which are both on an FCC lattice. The dendrite shown in c & d use the same parameters as the Wulff shapes in a & b respectively. These crystals each contain approximately 5×10^6 atoms, with the inset showing an atomic resolution close-up.

counting model, i.e. longer range or multi-body interactions would appear to be necessary.

Recall that Haxhimali et al. [8] examined the effects of anisotropy in the solid-liquid interfacial free-energy for a class of functions given by a truncated expansion in terms of cubic harmonics:

$$\gamma_c(\theta, \phi) = \gamma_0[1 + \epsilon_1 K_1(\theta, \phi) + \epsilon_2 K_2(\theta, \phi)], \tag{12}$$

where K_i is the ith cubic harmonic function [9]. One of the more intriguing shapes uncovered in these simulations, was a twelve armed dendrite that occurred when the K_1 contribution was absent, specifically for $\gamma_c(\hat{n}) = 1 - 0.02K_2(\hat{\mathbf{n}})$.

In an attempt to grow a crystal with a similar morphology using a KMC model, we first sought parameters that would give a similar functional form for γ_b. Like the spherical harmonics, cubic harmonics are orthonormal with respect to the inner product $\langle f, g \rangle = \frac{1}{4\pi} \int_{\partial B(0,1)} f \cdot g \, \mathrm{d}S$. This means any γ-plot, including γ_b of a bond-counting model, can be projected onto the set of all cubic harmonics K_i by:

$$\gamma_b(\hat{\mathbf{n}}) = \gamma_0(1 + \epsilon_1 K_1(\hat{n}) + \epsilon_2 K_2(\hat{n}) + \cdots), \tag{13}$$

where $\gamma_0 = \langle \gamma, 1 \rangle$ is the average value of γ_b and $\epsilon_i = \frac{1}{\gamma_0} \langle \gamma, K_i \rangle$. Thus, we computed ϵ_1 and ϵ_2 for energies of the form (7) as a function of the next-nearest-neighbor bond strength (with

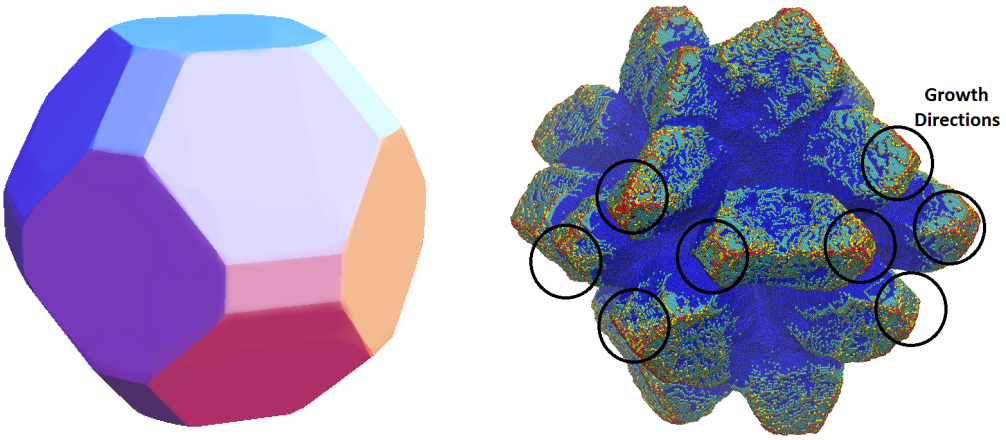

(a) (b)

Figure 7: The Wulff shape and resulting growth shape for a bond-counting model with $w_1 = 1$ and $w_2 = 0.353553$. These values been chosen to eliminate ϵ_1 in the cubic harmonic expansion of the surface energy (13). The Wulff shape in (a) has octagonal faces in the $\langle 100 \rangle$ directions, rectangular faces in the $\langle 110 \rangle$ directions, and hexagonal faces in the $\langle 111 \rangle$ directions. The dendrite in (b) contains approximately 5 million atoms. Note that there are 24 primary branches (six groups of four) that seem to be merging into six larger branches.

the weight for nearest-neighbor bonds fixed at 1). The bond strength $w_2 = 0.353553$ gives $\epsilon_1 = 0$ and $\epsilon_2 = -0.0219097$, and therefore seems to be a good candidate for growing a twelve-armed dendrite.

Next, we consider a KMC simulation using this value of w_2. The result shown in Fig. 7b is a dendrite containing approximately 5×10^6 atoms. Rather than a 12-armed dendrite, there are 24 primary branches that eventually merge in groups of four to form six larger branches. Haxhimali et al. did exhibit some 24-branched structures computed using non-zero values of ϵ_1, and the 12-armed structure in their model seemed to correlate with small values of ϵ_1. In fact, the 24-armed dendrites illustrated in their paper have branches that tighten in groups of four as ϵ_1 approaches 0.15, similar to the branches in our simulation.

To understand why this might be the case, we examine the Wulff shapes corresponding to the surface energy functions for both models. The first Wulff shape is shown on the far left in Fig. 8 and corresponds to $\gamma_c(\hat{n}) = 1 - 0.2K_2(\hat{n})$, where $\epsilon_1 = 0$ and all harmonics beyond ϵ_2 are also zero. This surface energy matches that used by Haxhimali et al. [8] for the 12-armed dendrite shown in their Fig. 2(e). The second Wulff shape is shown in Fig. 7a and corresponds to $\gamma_b(\hat{n}) = 1 - 0.2K_2(\hat{n}) + \cdots$, which is a surface energy for a bond-counting model with $\epsilon_1 = 0$ as a result of the choice $w_2 = 0.353553$. Note that the higher order harmonics are not necessarily zero, which accounts for the significant qualitative change in shape. In the γ_c Wulff shape there are twelve corners while the γ_b shape is faceted with twelve smaller facets corresponding to the corners in the former.

First we note that, since the first two cubic harmonic terms match in the two energies, the difference must be in the higher-order terms. Since the continuum model truncates after the second term, all higher-order coefficients are 0. In the expansion of γ_b, however, we can

compute these coefficients directly using (13):

$$\epsilon_3 = -0.0150347, \epsilon_4 = 0.00150363, \epsilon_5 = -0.00665085. \tag{14}$$

We have also considered how many terms the expansion of γ_c would need in order to see a Wulff shape for a continuum model similar to that of our bond-counting models. Using the computed coefficients of the cubic harmonic expansion of γ_b above, we computed the Wulff shapes for energies of the form $\sum_{i=1}^{n} \epsilon_i K_i(\hat{\mathbf{n}})$ for $n > 2$. It is interesting that just by adding the third term in the expansion, the Wulff shape is significantly more faceted. However, it is only when the expansion includes the first five terms that the Wulff shape becomes fully faceted and a very good approximation of γ_b as shown in Fig. 8.

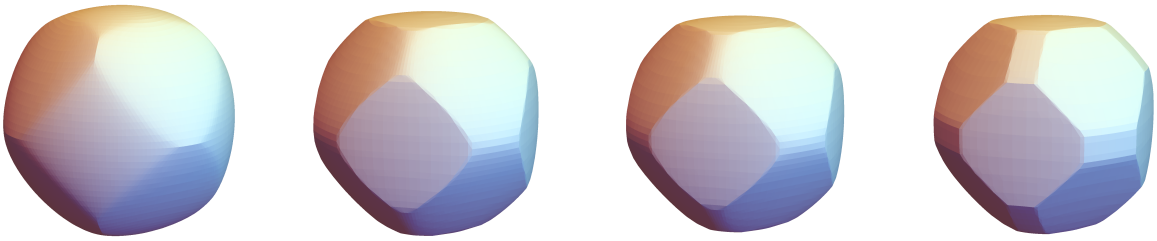

(a) $n = 2$ (b) $n = 3$ (c) $n = 4$ (d) $n = 5$

Figure 8: Wulff shapes corresponding to surface energy $\gamma(\hat{\mathbf{n}}) = 1 + \sum_{i=1}^{n} \epsilon_i K_i$ for $n = 2, 3, 4, 5$ using coefficient values in (14). The Wulff shape on the far left corresponds to the surface energy given by $\gamma_c(\hat{n}) = 1 - 0.02K_2(\hat{n})$ utilized by Haxhimali et al. [8].

6 Conclusion

Ultimately, we conclude that, at any finite level of approximation, both models exhibit a type of truncation error that makes them incompatible. In the continuum models, surface energy is modeled by truncating after one or more cubic harmonic terms. In bond-counting models, surface energy is the result of interactions between nearest-neighbors lying within some cutoff radius. It appears that a surface energy function within one of these families may lead to growth behavior not exhibited by functions in the other family using their respective models.

Acknowledgments

This work was supported by the National Science Foundation through grants DMS–1108643 and DMS–1613729. The authors are grateful to Jeff Hoyt, Selim Esedoglu, and Peter Smereka for helpful discussions related to this work.

References

[1] T. Witten and L. Sander, "Diffusion-limited aggregation, a kinetic critical phenomenon," *Phys. Rev. Lett.*, vol. 47, 1981.

[2] T. Vicsek, "Pattern formation in diffusion-limited aggregation," *Phys. Rev. Lett.*, vol. 53, pp. 2281–2284, 1984.

[3] O. Shochet, K. Kassner, E. Ben-Jacob, S. Lipson, and H. Muller-Krumbhaar, "Morphology transitions during non-equilibrium growth," *Physica A*, vol. 181, 1992.

[4] R. Harris and M. Grant, "Monte carlo simulation of a kinetic ising model for dendritic growth," *J. Phys. A: Math. Gen.*, vol. 23, pp. 567–571, 1990.

[5] Y. Saito and T. Ueta, "Monte carlo studies of equilibrium and growth shapes of a crystal," *Phys. Rev. A*, vol. 40, pp. 3408–3419, 1989.

[6] L. Jorgenson, R. Harris, M. Grant, and H. Guo, "Monte carlo simulation studies of dendritic instabilities in three dimensions," *Phys. Rev. E*, vol. 47, pp. 1235–1242, 1993.

[7] T. Schulze, "Simulation of dendritic growth into an undercooled melt using kinetic monte carlo techniques," *Physical Review E*, vol. 78, no. 020601, 2008.

[8] T. Haxhimal, A. Karma, F. Gonzales, and M. Rappaz, "Orientation selection in dendritic evolution," *Nature Materials*, vol. 5, pp. 660–664, 2006.

[9] J. J. Hoyt, M. Asta, and A. Karma, "Atomistic and continuum modeling of dendritic solidification," *Mater. Sci. Eng. R*, vol. 41, pp. 121–163, 2003.

[10] A. Voter, "Introduction to the kinetic monte carlo method," *Radiation Effects in Solids*, pp. 1–23, 2007.

[11] W. W. Mullins and R. F. Sekerka, "Morphological stability of a particle growing by diffusion or heat flow," *J. Appl. Phys.*, vol. 34, p. 323, 1963.

[12] T. Schulze, "Efficient kinetic monte carlo simulation," *Journal of Computational Physics*, vol. 227, pp. 2455–2462, 2008.

[13] J. Mackenzie, A. Moore, and J. Nicholas, "Bonds broken at atomically flat crystal surfaces i: Face-centered and body-centered cubic crystals," *J. Phys. Chem. Solids*, vol. 23, pp. 185–196, 1962.

[14] Y. Luo and R. Qin, "Influences of the third and fourth nearest neighboring interactions on the surface anisotropy of face-centered-cubic metals," *Surface Science*, vol. 624, pp. 103–111, 2014.

[15] I. Fonseca, "The wulff theorem revisited," *Proc. Roy. Soc. London A*, vol. 432, pp. 125–145, 1991.

[16] S. Davis, *Theory of Solidification*. Cambridge University Press, 2001.

[17] W. Wang, D. Wang, X. Liu, Q. Peng, and Y. Li, "Ptni nanodendrites with high hydrogenation activity," *Chem. Commun.*, vol. 49, pp. 2903–2905, 2013.

[18] G. Jiang, L. Wang, T. Chen, J. Yu, and J. Wang, "Preparation and characterization of dendritic silver nanoparticles," *J. Mater. Sci.*, vol. 40, pp. 1681–1683, 2005.